Multi-Objective Optimization of Capacitive Wireless Power Transfer Systems for Electric Vehicle Charging

Kate Doubleday, Ashish Kumar, Brandon Regensburger, Saad Pervaiz, Sreyam Sinha,
Zoya Popovic, and Khurram K. Afridi
Department of Electrical, Computer, and Energy Engineering
University of Colorado Boulder
Boulder, Colorado 80309

***Abstract*—This paper presents a methodology for multi-objective optimization of capacitive wireless power transfer (WPT) systems for electric vehicle charging that allows for a favorable tradeoff between power transfer density and efficiency. By quantifying the tradeoff between these two objectives, this multi-objective optimization approach can inform engineering decisions, given the requirements of a particular charging application. The capacitive WPT system considered in this paper utilizes L-section matching networks with air-core inductors and capacitors realized using the parasitic capacitances of the system. The proposed optimization methodology incorporates constraints on achievable matching network capacitances, realizable inductor designs, and fringing electric fields set by safety considerations. The models used in the optimization methodology are validated using a 12-cm air-gap 6.78-MHz prototype capacitive WPT system, which transfers 589 W, achieving a power transfer density of 19.6 kW/m^2 and an efficiency of 88.2%.**

***Index Terms*—Wireless power transfer; capacitive wireless power transfer; multi-objective optimization; power transfer density; efficiency**

I. Introduction

Wireless power transfer (WPT) systems for electric vehicle (EV) charging typically utilize magnetic coupling to transfer energy from a coil on the ground to a coil on the vehicle. Unfortunately, these inductive WPT systems require bulky and expensive ferrites for flux guidance, which also limit operating frequency (and hence size) due to core losses [1]. An emerging alternative is capacitive WPT, which utilizes electric fields to transfer energy between two pairs of metal plates separated by an air-gap, as shown in Fig. 1. Capacitive WPT systems do not require ferrites and can be operated efficiently at high frequencies. Hence, they have the potential to achieve higher power transfer densities and efficiencies than inductive WPT systems. Additionally, due to the directed nature of electric fields, their tolerance to misalignment is higher than that of inductive systems [2]. However, capacitive WPT has mainly been utilized in applications with small air gaps [3], [4], owing to the large capacitive reactance of large air-gaps that is difficult to efficiently compensate. This challenge has recently been addressed using various matching network topologies,

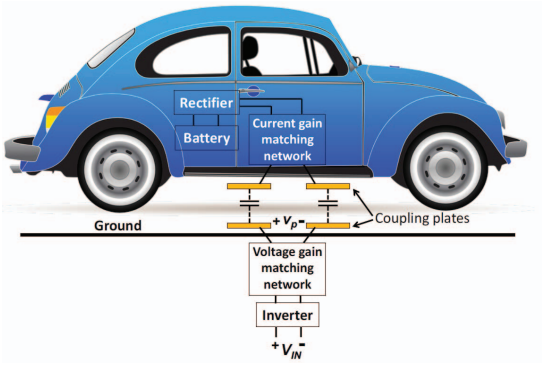

Fig. 1. A capacitive wireless power transfer system for EV charging.

with work on large air-gap capacitive WPT suitable for EV charging applications being reported in [2], [5]–[11].

The design of a capacitive WPT system involves the selection of a number of parameters, such as the size and lateral spacing of the coupling plates, with each choice resulting in solutions delivering different performance in terms of desirable objectives. The critical objectives may include maximizing system efficiency, minimizing the system volume or weight, maximizing power transfer density to minimize the system's footprint under the vehicle chassis, or complying with other application-specific requirements. In order to select the most appropriate design for a particular application, a methodology is needed to optimize across the multiple target objectives. This paper presents a multi-objective optimization methodology for capacitive WPT systems to help identify designs that provide a favorable tradeoff between power transfer density and efficiency. The capacitive WPT system considered in this paper utilizes L-section matching networks with air-core inductors and capacitors realized using the parasitic capacitances of the system. This optimization methodology incorporates constraints imposed by achievable matching network capacitances, realizable inductor designs, and fringing electric field safety standards [12], [13]. The methodology simultaneously determines the circuit parameters and the system geometry by employing empirically-derived relationships between the geometry and its electromagnetic behavior.

978-1-5090-5326-1/17/$31.00 ©2017 IEEE

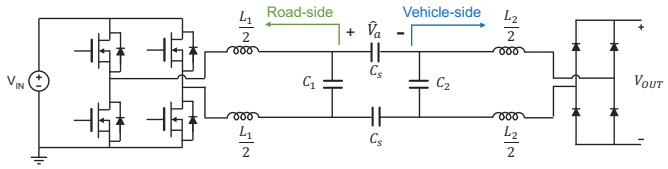

Fig. 2. An example circuit implementation of a capacitive wireless power transfer system for EV charging.

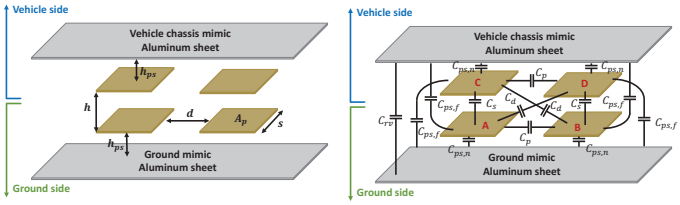

(a) (b)

Fig. 3. Capacitive WPT system's coupling plates: (a) geometric parameters, and (b) capacitance model including the 2 coupling capacitances and 13 parasitic capacitances present in an EV charging application.

The remainder of the paper is organized as follows: Section II introduces the design parameters. Section III describes the capacitive coupling plate model. Section IV develops a model to account for fringing field safety limits. Section V describes the proposed multi-objective optimization methodology. Section VI presents the optimization results. Section VII reports experimental results validating the optimization models for a 589-W capacitive WPT system. Finally, Section VIII concludes the paper.

II. Capacitive WPT System Design Parameters

One possible implementation of the capacitive WPT system of Fig. 1 is shown in Fig. 2. The system includes a full-bridge high-frequency inverter, which feeds the system's ground-side coupling plates through a matching network. This single-stage, L-section matching network provides voltage gain and partially compensates for the coupler's large capacitive reactance. By stepping up the voltage applied to the plates, it limits the displacement current and the voltage across the air gap, hence, limiting fringing fields. The system's vehicle-side coupling plates are followed by a single-stage L-section current gain matching network, which provides the remaining compensation and steps up the current to the level required to charge the vehicle battery. Lastly, a high-frequency full-bridge rectifier interfaces the system to the vehicle battery.

The geometry of the capacitive WPT system considered here is shown in Fig. 3(a), including the definition of its geometric parameters. The system has four square coupling plates with area A_p and side length $s = \sqrt{A_p}$, two of which are ground-side transmitting plates and two are vehicle-side receiving plates, separated by an air-gap of height h. The system's plates are laterally separated by a distance d. The sheets above and below the coupling plate array represent the vehicle chassis and the ground, and are assumed to have the dimensions of a typical passenger vehicle. The plate-to-sheet gap has height h_{ps}.

Figure 3(b) shows all the capacitances associated with this capacitive WPT system, including parasitic capacitances which capture incidental coupling amongst the coupling plates as well as the capacitive coupling between the plates and the vehicle chassis and roadway. These parasitics, if not taken into consideration, can negatively impact the power transfer across the air-gap. The objective of the design procedure proposed in Section V is to determine the system's geometric parameters, as well as the circuit parameters of Fig. 2, to achieve a high efficiency, high power transfer density capacitive WPT system

TABLE I
Capacitive WPT System Design Parameters and Allowable Minimum and Maximum Values

Design Parameter		Minimum	Maximum
A_p	Square coupling plate area	25 cm^2	625 cm^2
d	Lateral plate-to-plate distance	5 cm	25 cm
h_{ps}	Plate-to-sheet height	0.2 cm	2 cm
V_{OUT}	Output (and input) voltage	100 V	400 V

in the presence of these significant parasitics. These geometric and electrical design parameters are listed in Table I. For this analysis, a few parameters are held constant: the air-gap height is selected as 12 cm, the operating frequency is 6.78 MHz (i.e., within an ISM-band), and the input voltage is always selected to equal the output voltage for system symmetry. The next section derives an equivalent circuit model from the system geometry to relate the geometric parameters in Fig. 3(a) to the capacitances of Fig. 3(b), enabling selection of the remaining system parameters.

III. Coupling Plate Equivalent Model

Figure 4(a) shows the circuit schematic of Fig. 2 with the parasitic capacitances of the WPT system incorporated. The number of capacitances in this circuit model can be reduced, as discussed below. To begin the capacitance reduction, note that the matching network inductances, L_1 and L_2, are each split between the forward and return paths, resulting in a symmetric circuit. In this symmetric circuit, there is zero voltage across the capacitance between the road and the vehicle chassis, C_{rv}, shown in grey. As such, no parasitic current flows through this capacitance, and it can be ignored. The remainder can be simplified by two-port theory and series and parallel combinations to the four equivalent capacitances shown in Fig. 4(b). Also note that this simplified model improves the capacitive WPT system design by realizing the matching network capacitances entirely with the existing parasitics, eliminating the need for discrete on-board capacitors C_1 and C_2, which are lossy and susceptible to breakdown. Details of this simplification process are reported in [11].

The equivalent capacitances shown in Fig. 4(b) can be expressed in terms of the original capacitances of Fig. 4(a) as

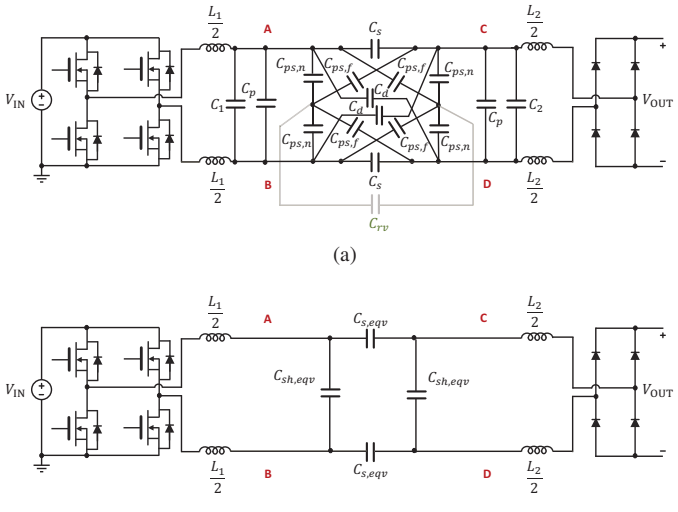

Fig. 4. (a) Implementation of the capacitive WPT system, including the 13 parasitic capacitances present in an EV charging application. (b) Due to the symmetrically split inductors, the parasitic capacitances can be modeled as an equivalent 4-capacitance system, and the design can be further improved by realizing the matching network capacitances entirely with the existing parasitics.

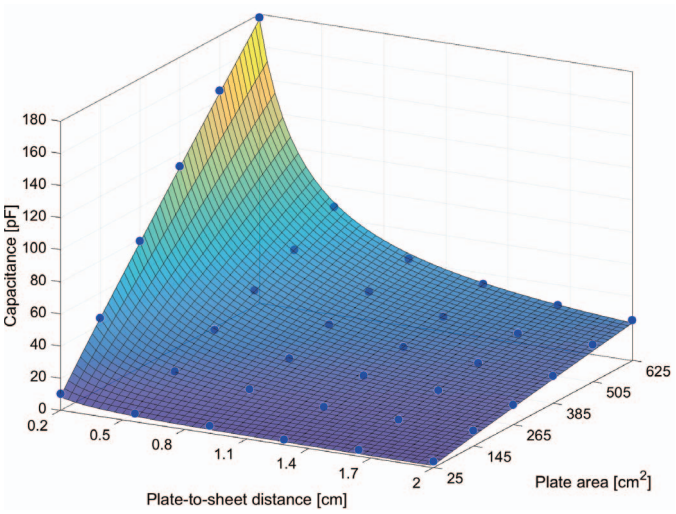

Fig. 5. Empirical fit of the equivalent shunt capacitance, $C_{sh,eqv}$, calculated through HFSS simulations over the intended range of plate areas and plate-to-sheet heights, and shown here for one value of the lateral plate-to-plate distance. Blue dots indicate the discrete HFSS simulated results calculated by (1), and the surface plots the empirical fit reported in (4).

follows. The equivalent shunt capacitance, $C_{sh,eqv}$, is given by:

$$C_{sh,eqv} = C_p + \frac{C_{ps,n}}{2} + \frac{C_{ps,f}}{2} + C_d. \tag{1}$$

Similarly, the equivalent series capacitance $C_{s,eqv}$ of the 4-capacitance model can be expressed as:

$$C_{s,eqv} = C_s - C_d. \tag{2}$$

For the design optimization procedure, it is desirable to determine approximations to the values of the capacitances used in (1) and (2) that capture their dependencies on the geometric parameters. To that end, 216 ANSYS HFSS simulations of the aluminum sheets and coupling plates were conducted at 6.78 MHz operating frequency, over the following parameter ranges: square plate areas from 25 cm^2 to 625 cm^2; lateral plate-to-plate distances from 5 cm to 25 cm; and plate-to-sheet heights from 0.2 cm to 2 cm.

Note that in an electric vehicle application, where the plate-to-sheet height would typically be much smaller than the other geometric dimensions, the capacitance from a coupling plate to the nearest sheet, $C_{ps,n}$, is the largest of the capacitances in Fig. 3(b). Therefore, the equivalent shunt capacitance $C_{sh,eqv}$ is dominated by the factor $\frac{C_{ps,n}}{2}$, and can be well approximated as:

$$C_{sh,eqv} \approx \frac{C_{ps,n}}{2}. \tag{3}$$

This intuition can be quantitatively confirmed by fitting a function to the results of the HFSS simulations, as shown in Fig. 5 for the case where the lateral plate-to-plate distance is 5 cm. The proposed fit equation takes the form:

$$C_{sh,eqv} \approx \frac{1}{2}\frac{\epsilon_0 A_p}{h_{ps}}\left[1 + \alpha\left(\frac{h_{ps}}{s}\right)^{\beta}\right], \tag{4}$$

where ϵ_0 is the permittivity of free space, and α and β are dimensionless fitting parameters. It can be seen that (4) captures the capacitance $\frac{C_{ps,n}}{2}$ of (3) as the sum of two terms, one that equals the ideal parallel-plate capacitance between the coupling plate and ground or vehicle mimic sheet, and another that accounts for the additional capacitance generated by the fringing fields between the coupling plate and the much larger sheet. For fitting parameter values of $\alpha = 0.774$ and $\beta = 0.170$, the R-squared value of the fit given in (4) is at least 0.992 for each considered value of the plate-to-plate distance.

Similarly, the equivalent series capacitance of (2) is approximated by an empirical fit of the form:

$$C_{s,eqv} \approx \frac{\epsilon_0 A_p}{h}\left[1 - \frac{k}{\sqrt{\left(\frac{d+s}{h}\right)^2 + 1}}\right], \tag{5}$$

where k is a dimensionless fitting parameter. The first term in (5) represents the parallel-plate model of the series capacitance C_s, and the second term approximates the diagonal capacitance C_d, with the fitting parameter k capturing the misalignment and fringing between diagonal plates. Figure 6 shows this function fit to the HFSS results for (2), for one value of the plate-to-sheet height. In contrast to the equivalent shunt capacitance, the equivalent series capacitance is a stronger function of the lateral plate-to-plate distance than the plate-to-sheet height. With $k = 0.745$, the R-squared value of the fit given in (5) is at least 0.954 for each value in the range of plate-to-sheet heights considered. These empirical fit equations will be utilized in the multi-objective optimization approach described in Section V to achieve the desired capacitance values by modifying the system geometry.

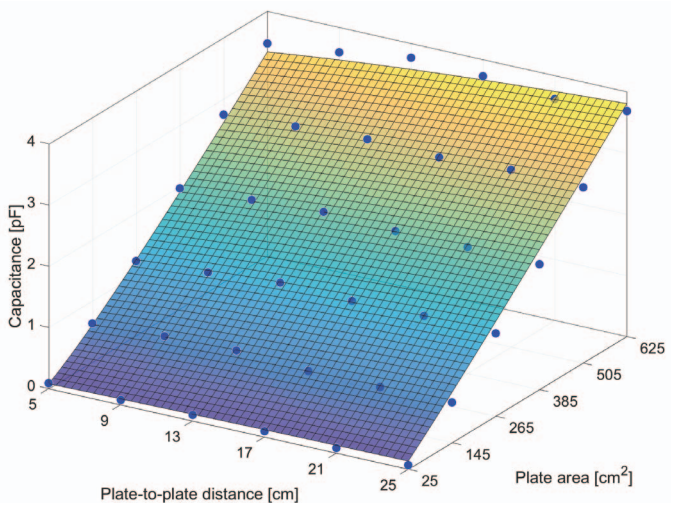

Fig. 6. Empirical fit of the equivalent series capacitance, $C_{s,eqv}$, calculated through HFSS simulations over the intended range of plate areas and plate-to-plate distances, and shown here for a plate-to-sheet height of 0.92 cm. Blue dots indicate the discrete HFSS simulated results calculated by (2), and the surface plots the empirical fit reported in (5).

IV. Fringing Field Constraint Modeling

Safety standards require the electric fields generated by the capacitive WPT system to be below a certain limit, E_{limit}, in regions beyond the edge of the vehicle chassis [12]. At the operating frequency of 6.78 MHz, this limit is 33.4 $\mathrm{V/m}$ [13]. This fringing field limit should be incorporated into the optimization methodology. In particular, the safety constraint should be applied as a limit on the air-gap voltage magnitude, $|\hat{V}_a|$, shown in Fig. 2. A simulated model of the fringing field behavior is developed here to relate the maximum air-gap voltage magnitude to the system geometry.

The air-gap voltage constraint is derived using simulations over the range of plate areas given in Table I. First, as shown in Fig. 7(a), the system geometry is simulated in Ansys Maxwell with a voltage excitation of magnitude $\pm V_{test}/2$ on each copper plate, so that the total air-gap voltage is the test voltage, V_{test}. Assuming the fringing field magnitude is maximal at half the air-gap height [5], the fringing electric field behavior is characterized along a line at this height, from the edge of the copper plate outward past the edge of the chassis. The electric field, E_{test}, is determined at the edge of the chassis for the particular system geometry; Fig. 7(b) shows an example. As the electric field scales linearly with the applied voltage, the maximum air-gap voltage for a given plate size can then be determined as:

$$V_{max} = \frac{E_{limit}}{E_{test}} V_{test} \tag{6}$$

This maximum air-gap voltage calculation was performed for 36 Ansys Maxwell simulations over the ranges of plate area and lateral plate-to-plate distance listed in Table I. The results are reported in Fig. 8. As can be seen, the plate size has a strong impact on the maximum allowable air-gap voltage. However, the lateral plate-to-plate distance has only a minor

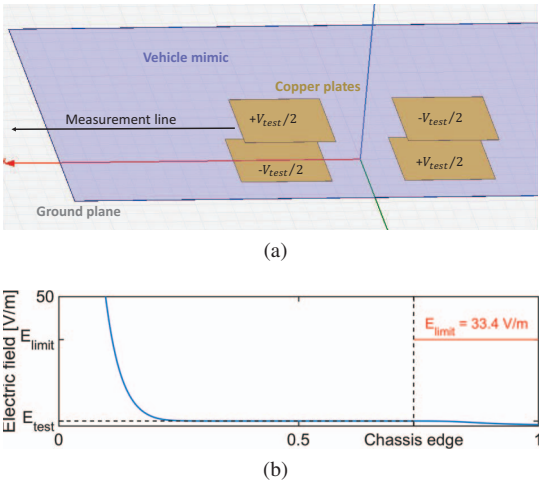

Fig. 7. (a) Ansys Maxwell simulation of the system with a test voltage across the air-gap determines the fringing field along the measurement line. (b) An example of the electric field behavior from the edge of the copper plate outwards, which is used to determine E_{test} at the chassis edge.

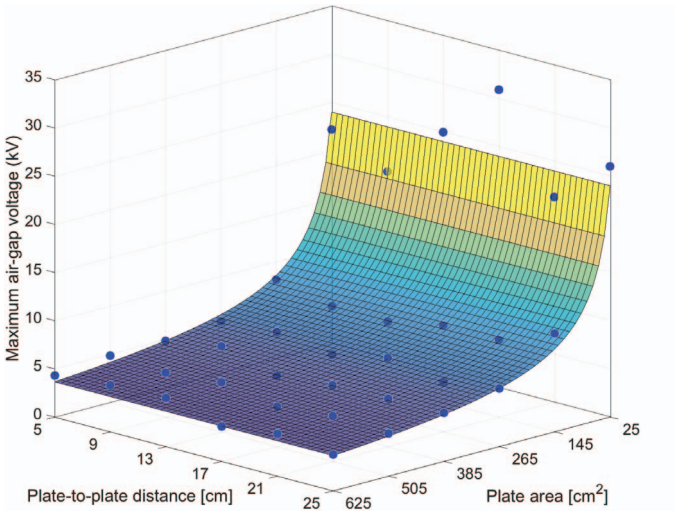

Fig. 8. Empirical fit of the maximum allowable air-gap voltage, $|\hat{V}_a|$, calculated through HFSS simulations over the intended range of plate areas and plate-to-plate distances, at the minimum plate-to-sheet height of 0.2 cm. Blue dots indicate the Ansys Maxwell simulated results calculated by (6), and the surface plots the empirical fit reported in (7).

impact on the maximum air-gap voltage for the geometries considered here. From these results, the maximum air-gap voltage can be approximated solely as a function of plate area as:

$$|\hat{V}_a| = V_{max} \approx \frac{k_v}{A_p^{\delta}}. \tag{7}$$

Here, k_v and δ are fitting parameters. For $k_v = 724$ and $\delta = 0.584$, the proposed fit has an R-squared value of 0.945. In the next section, the empirical equations developed in this and the previous sections are incorporated in the multi-objective optimization methodology to generate designs that can comply with the real-world constraints of an EV charging application.

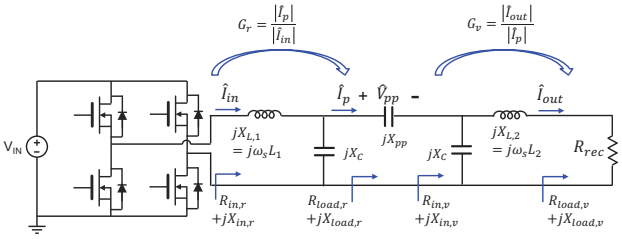

Fig. 9. Analytical framework used to describe the desired circuit behavior in the optimization procedure.

V. Multi-Objective Optimization Methodology

A multi-objective optimization methodology is presented here to inform the selection of the capacitive WPT system's geometric and electrical parameters. Here, the desired objectives are to maximize the system efficiency and the power transfer density, though the methodology can be readily extended to evaluate other objectives. The power transfer density (PTD) is defined in terms of the total plate area and the output power, P_{OUT}, as PTD $= P_{OUT}/2A_p$. In the case where the capacitive WPT system losses are dominated by the matching network losses [9], the efficiency of the matching networks is used as a proxy for the overall system efficiency. Furthermore, since the matching networks do not utilize discrete capacitors, the proposed optimization methodology estimates their losses based on the inductor losses. Therefore, the two objective functions related to power transfer density and efficiency can equivalently be evaluated by minimizing the square plate area, A_p, and minimizing the matching network losses, P_{loss}, respectively. Since in this case one of the decision variables, plate area, is equal to an objective function, the Pareto front is evaluated iteratively by minimizing matching network losses over a selection of plate areas using Matlab's Global Optimization Toolbox.

In order to evaluate the matching network losses of a prospective design, the matching network analysis method presented in [14], [15] is applied to describe the circuit relationships and behavior. The critical circuit quantities in this framework are shown in Fig. 9, which simplifies Fig. 4(b) by combining series components and applying fundamental-frequency approximation to model the rectifier as a resistor. Throughout, the subscripts r and v refer to the road-side and vehicle-side quantities, respectively.

The desired circuit behavior is described through this framework by relating the component values to the desired matching network current gains (G_r and G_v) and input and output impedances. First, under fundamental-frequency approximation, the vehicle-side matching network is loaded by an effective resistance, given by:

$$R_{load,v} = R_{rec} = \frac{8}{\pi^2}\frac{V_{OUT}^2}{P_{OUT}}, \qquad X_{load,v} = 0. \tag{8}$$

Furthermore, it is desired to make the input impedance of the road-side matching network inductive enough to achieve zero-voltage switching (ZVS) of the inverter transistors. It can be shown that ZVS can be achieved with minimal circulating currents if the input impedance of the road-side matching network satisfies the following relationship [9]:

$$\frac{X_{in,r}}{R_{in,r}} = \tan\left(\cos^{-1}\frac{1}{1+\frac{8C_{oss}V_{IN}^2 f_s}{P_{OUT}}}\right) \tag{9}$$

Here, C_{oss} is the linear equivalent output capacitance of the inverter transistors, V_{IN} is the dc input voltage of the system, and f_s is its operating frequency. The two matching networks are related to each other through the coupling plates as:

$$R_{load,r} = R_{in,v}, \qquad X_{load,r} = X_{pp} + X_{in,v}, \tag{10}$$

where the combined plate impedance X_{pp} is determined by the empirical fit of (5), as:

$$X_{pp} = \frac{-2}{\omega_s \frac{\epsilon_0 A_p}{h}\left[1 - \frac{k}{\sqrt{\left(\frac{d+s}{h}\right)^2+1}}\right]}, \tag{11}$$

where $\omega_s = 2\pi f_s$.

The input and output impedances of the two matching networks can also be related to each other and to the reactive component values, as shown in [14], [15]:

$$R_{in,r} = R_{load,r}\frac{X_C^2}{[R_{load,r}^2 + (X_{load,r}+X_C)^2]}, \tag{12}$$

$$X_{in,r} = X_{L,1} + X_C\frac{[R_{load,r}^2 + X_{load,r}(X_{load,r}+X_C)]}{[R_{load,r}^2 + (X_{load,r}+X_C)^2]}, \tag{13}$$

$$R_{in,v} = R_{load,v}\frac{X_C^2}{[R_{load,v}^2 + (X_{load,v}+X_C+X_{L,2})^2]}, \tag{14}$$

$$X_{in,v} = X_C \times \frac{[R_{load,v}^2 + (X_{load,v}+X_{L,2})(X_{load,v}+X_C+X_{L,2})]}{[R_{load,v}^2 + (X_{load,v}+X_C+X_{L,2})^2]}, \tag{15}$$

where $X_{L,1}$ and $X_{L,2}$ are the total inductive reactances of the matching networks (including the two split inductors in each network), and X_C is the capacitive reactance of the equivalent shunt capacitance of (4), given by:

$$X_C = \frac{-1}{\omega_s \frac{1}{2}\frac{\epsilon_0 A_p}{h_{ps}}\left[1 + \alpha\left(\frac{h_{ps}}{s}\right)^\beta\right]} \tag{16}$$

In addition, this analysis framework relates the current gain of each matching network to its component values and input and output impedances as:

$$G_r = \sqrt{\frac{X_C^2}{R_{load,r}^2 + (X_{load,r}+X_C)^2}}, \tag{17}$$

$$G_v = \sqrt{\frac{X_C^2}{R_{load,v}^2 + (X_{load,v}+X_C+X_{L,2})^2}}. \tag{18}$$

Furthermore, these current gains can be expressed by definition under fundamental-frequency approximation as:

$$G_r = \frac{|\hat{I}_p|}{|\hat{I}_{in}|} = \frac{\frac{|\hat{V}_{pp}|}{|Xpp|}}{\frac{\pi P_{IN}}{2V_{IN}}}, \qquad G_v = \frac{|\hat{I}_{out}|}{|\hat{I}_p|} = \frac{\frac{\pi P_{OUT}}{2V_{OUT}}}{\frac{|\hat{V}_{pp}|}{|Xpp|}}. \tag{19}$$

In this study, the input power, P_{IN}, is assumed to equal the output power. However, iteratively adjusting the input power based on the current efficiency estimate can improve this approximation.

Next, a constraint is included to consider only feasible matching network inductance values. The quality factor Q_L of the inductors must be high enough for the system to achieve a minimum desired efficiency, and the self-resonant frequency (SRF) of the inductors must be sufficiently higher than the system's operating frequency. These Q_L and SRF requirements impose an upper limit on the maximum realizable inductance values [7]. To achieve a Q_L of ~300, a maximum realizable inductance value of $L_{max} = 65\,\mu\text{H}$ is selected to maintain an ample margin between the operating frequency and SRF.

Lastly, the power losses can be estimated from the inductor losses as:

$$P_{loss} = \frac{|\hat{I}_{in}|^2}{2}\frac{X_{L,1}}{Q_L} + \frac{|\hat{I}_{out}|^2}{2}\frac{X_{L,2}}{Q_L} \tag{20}$$

Finally, by combining (8)-(20), the matching network loss minimization problem can be expressed as the following constrained optimization problem:

$$\min_{\{L_1, L_2, h_{ps}, d, V_{OUT}, |\hat{V}_a|\}} \quad P_{loss} \tag{21}$$

$$\text{s.t.} \quad 0 < L_1, L_2 < L_{max} \tag{22}$$

$$h_{ps,min} < h_{ps} < h_{ps,max} \tag{23}$$

$$d_{min} < d < d_{max} \tag{24}$$

$$V_{OUT,min} < V_{OUT} < V_{OUT,max} \tag{25}$$

$$0 < |\hat{V}_{pp}| < 2\frac{k_v}{A_p^{\delta}} \tag{26}$$

$$\frac{\frac{|\hat{V}_{pp}|}{|Xpp|}}{\frac{\pi P_{IN}}{2V_{IN}}} = \sqrt{\frac{X_C^2}{R_{load,r}^2 + (X_{load,r} + X_C)^2}} \tag{27}$$

$$\frac{\frac{\pi P_{OUT}}{2V_{OUT}}}{\frac{|\hat{V}_{pp}|}{|Xpp|}} = \sqrt{\frac{X_C^2}{R_{load,v}^2 + (X_{load,v} + X_C + X_{L,2})^2}} \tag{28}$$

$$\frac{X_{in,r}}{R_{in,r}} = \tan\left(\cos^{-1}\frac{1}{1 + \frac{8C_{oss}V_{IN}^2 f_s}{P_{OUT}}}\right) \tag{29}$$

As can be seen, (23)-(25) represent the parameter ranges defined in Table I, and (26) captures the fringing field constraint. By repeating the optimization process over a range of plate areas for a particular power level, the tradeoff between the two objectives – high efficiency and high power transfer density – can be quantified, as demonstrated below.

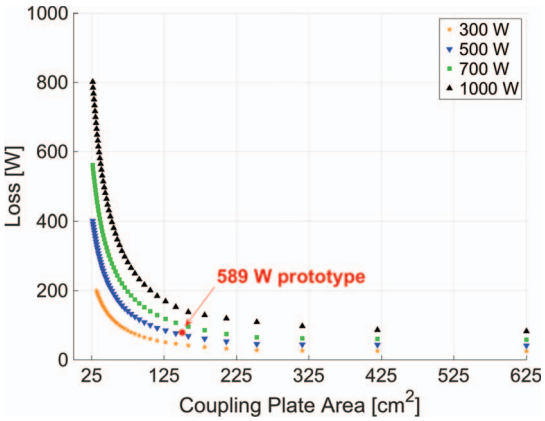

Fig. 10. Pareto front showing the tradeoff between minimizing power loss and minimizing plate area of the capacitive WPT system. Also indicated is the performance of the 589-W experimental prototype.

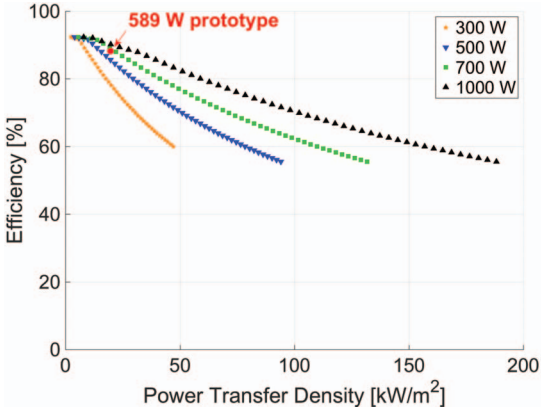

Fig. 11. The trade-off between maximizing power transfer density and maximizing efficiency of the capacitive WPT system is illustrated at different power levels. Also indicated is the performance of the 589-W experimental prototype.

VI. Multi-Objective Optimization Results

The optimization methodology outlined in the previous section is applied to the capacitive WPT system of Fig. 4(b), for output power levels ranging from 300 W to 1 kW, suitable for a single module of a multi-modular capacitive WPT system for electric vehicle charging [6], [7]. At each power level, the optimization is performed for 50 values of the coupling plate area to determine the tradeoff between minimizing plate area and minimizing power loss. The resulting Pareto fronts are shown in Fig. 10. As can be seen, low-loss systems can be achieved, but at the cost of large plate area, which increases the system's footprint under the vehicle chassis. At some point, increasing plate size further no longer provides a substantial reduction in power loss. The selection of a particular design will depend on the relative importance of these two objectives for the specific application.

The tradeoff between the two objectives can also be illustrated by transforming the results into the more familiar metrics of efficiency and power transfer density, as shown in Fig. 11. In this form, it can be noted that the curvature of

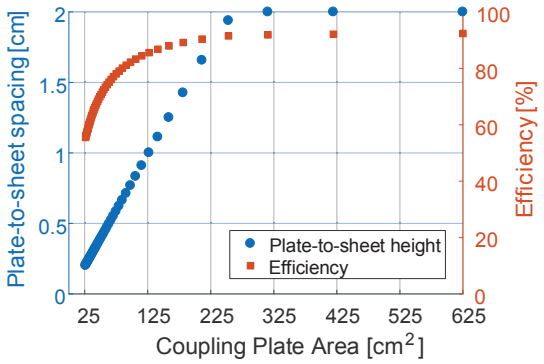

Fig. 12. Comparison of the selected plate-to-sheet height and the corresponding matching network efficiency for a 700-W capacitive WPT system.

the Pareto front changes as the power transfer density gets very small (i.e., as the plate area gets large). This behavior is caused by the maximum plate-to-sheet height limit of 2 cm. As shown in Fig. 12 for a 700-W system, the plate-to-sheet height limit forces a deviation from the best-case matching network design and slightly fore-shortens the natural taper in matching network efficiency as the plate size gets very large. The maximum inductance limit also has a major impact on the results by limiting the achievable compensation for the air gap. In fact, for the smallest plate areas, in which the air-gap capacitance is very small and thus its reactance is very large, the optimization does not converge to a feasible solution.

Some of the other practical constraints do not cause such major trends in the results – for instance, the maximum air-gap voltage is never reached in these Pareto-optimal designs. In contrast, the lateral plate-to-plate distance is selected at its maximum value of 25 cm for all scenarios to minimize the parasitic diagonal capacitance that degrades the equivalent series capacitance, $C_{s,eqv}$. Should the maximum limit on the lateral plate-to-plate distance be relaxed, there may reach a point where those two competing needs – minimizing parasitics and meeting the safety requirements – begin to interact and change the behavior of the results.

VII. Prototype Design and Experimental Validation

The models used in the proposed optimization methodology are experimentally validated using a 6.78-MHz 589-W prototype capacitive WPT system utilizing $150\,\mathrm{cm}^2$ ($12.25\,\mathrm{cm} \times 12.25\,\mathrm{cm}$) coupling plates. The schematic of this capacitive WPT system is shown in Fig. 13, and a photograph of the system is shown in Fig. 14. The aluminum sheets visible in Fig. 14 mimic the vehicle chassis and road. The full-bridge inverter is built using GS66506T enhancement-mode GaN FETs, and a 45.1 Ω resistor is used to model the rectifier and load (i.e., $R_{rec} = 45.1\,\Omega$). To compare to the models presented above, the selected geometric and electrical parameters of the experimental set-up are compared to the closest 500-W optimization scenario in Table II. To compare this prototype to the optimization designs that assume the presence of a full-bridge rectifier, fundamental frequency approximation is applied to

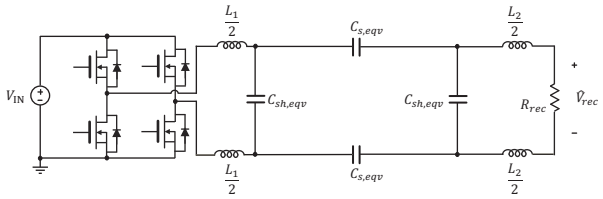

Fig. 13. Schematic of the 6.78-MHz, 589-W, 12-cm air-gap capacitive WPT prototype.

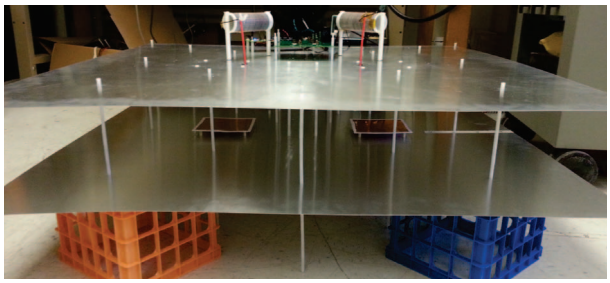

Fig. 14. Prototype 6.78-MHz, 589-W capacitive WPT system with copper coupling plates, aluminum sheets mimicking the road and vehicle chassis, inverter, and matching networks.

calculate the effective dc output voltage: $V_{OUT,eff} = \frac{\pi}{4}|\hat{V}_{rec}|$. The geometric and inductance values are all very close in value, though there is some discrepancy in the effective output voltage level – this discrepancy needs to be further investigated, possibly by estimating the air-gap voltage in the prototype system through a measurement of the air-gap displacement current.

The measured waveforms of the input voltage and current, inverter switch-node voltages, inverter output current and the system output voltage with the prototype operating at 589 W are shown in Fig. 15. The prototype system achieves a power transfer density of 19.6 kW/m^2 and an efficiency of 88.2%. For comparison, the optimization methodology predicts a matching network efficiency of 85.9% for the 500-W design shown in Table II, for inductor quality factors of ∼300.

VIII. Conclusion

This paper presents a multi-objective optimization methodology for capacitive WPT systems for electric vehicle charging, which investigates tradeoffs between power transfer density and efficiency. The considered capacitive WPT system employs L-section matching networks with air-core inductors and capacitors realized using the parasitic capacitances of the system. The proposed optimization methodology incorporates

TABLE II
Comparison of Simulated and Experimental Capacitive WPT System Parameters

	A_p	d	h_{ps}	V_{OUT}	L_1	L_2
Sim.	$159\,\mathrm{cm}^2$	25 cm	1.25 cm	284 V	65 µH	61.1 µH
Exp.	$150\,\mathrm{cm}^2$	23 cm	1.27 cm	184 V	62.9 µH	62.9 µH

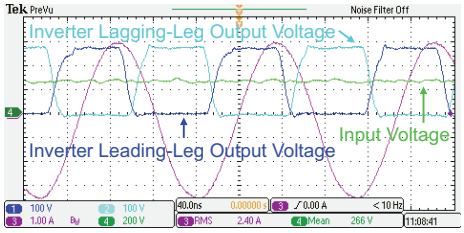

(a)

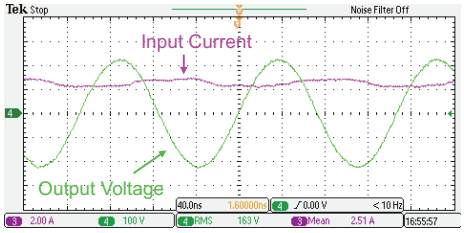

(b)

Fig. 15. Experimental waveforms: (a) dc input voltage, switch-node voltages, and inverter output current, and (b) dc input current and output voltage of the prototype converter operating at 589 W.

practical constraints including achievable matching network capacitances, realizable inductor designs, and fringing electric field limits set by safety considerations. By quantifying the tradeoff between efficiency and power transfer density, this multi-objective optimization can inform engineering decisions, given the requirements of a particular charging application. The models used in the optimization methodology are validated using a 12-cm air-gap 6.78-MHz prototype capacitive WPT system, which transfers 589 W of power, achieving a power transfer density of 19.6 $\mathrm{kW/m^2}$ and an efficiency of 88.2%.

Acknowledgment

The authors would like to acknowledge the financial support provided by the Advanced Research Projects Agency – Energy (ARPA-E), Department of Energy under Award Number DE-AR0000618.

References

[1] G. A. Covic and J. T. Boys, "Modern trends in inductive power transfer for transportation applications," *IEEE Journal of Emerging and Selected Topics in Power Electronics*, vol. 1, no. 1, pp. 28–41, March 2013.

[2] F. Lu, H. Zhang, H. Hofmann, and C. Mi, "A double-sided LCLC-compensated capacitive power transfer system for electric vehicle charging," *IEEE Transactions on Power Electronics*, vol. 30, no. 11, pp. 6011–6014, Nov 2015.

[3] J. Dai and D. C. Ludois, "A survey of wireless power transfer and a critical comparison of inductive and capacitive coupling for small gap applications," *IEEE Transactions on Power Electronics*, vol. 30, no. 11, pp. 6017–6029, Nov 2015.

[4] M. Kline, I. Izyumin, B. Boser, and S. Sanders, "Capacitive power transfer for contactless charging," *Proceedings of the IEEE Applied Power Electronics Conference and Exposition (APEC),* Fort Worth, TX, pp. 1398–1404, March 2011.

[5] A. Kumar, S. Pervaiz, C.-K. Chang, S. Korhummel, Z. Popovic, and K. K. Afridi, "Investigation of power transfer density enhancement in large air-gap capacitive wireless power transfer systems," *Proceedings of the IEEE Wireless Power Transfer Conference (WPTC),* Boulder, CO, pp. 1–4, May 2015.

[6] I. Ramos, K. Afridi, J. A. Estrada, and Z. Popovic, "Near-field capacitive wireless power transfer array with external field cancellation," *Proceedings of the IEEE Wireless Power Transfer Conference (WPTC),* Aviero, Portugal, pp. 1–4, May 2016.

[7] K. Doubleday, A. Kumar, S. Sinha, B. Regensburger, S. Pervaiz, and K. Afridi, "Design tradeoffs in a multi-modular capacitive wireless power transfer system," *Proceedings of the IEEE PELS Workshop on Emerging Technologies: Wireless Power Transfer (WoW),* Knoxville, TN, pp. 35–41, Oct 2016.

[8] F. Lu, H. Zhang, H. Hofmann, and C. C. Mi, "An inductive and capacitive combined wireless power transfer system with LC-compensated topology," *IEEE Transactions on Power Electronics*, vol. 31, no. 12, pp. 8471–8482, Dec 2016.

[9] B. Regensburger, A. Kumar, S. Sinha, K. Doubleday, S. Pervaiz, Z. Popovic, and K. Afridi, "High-performance large air-gap capacitive wireless power transfer system for electric vehicle charging," *Proceedings of the IEEE Transportation Electrification Conference and Expo (ITEC),* Chicago, IL, June 2017.

[10] H. Zhang, F. Lu, H. Hofmann, W. Liu, and C. Mi, "A six-plate capacitive coupler to reduce electric field emission in large air-gap capacitive power transfer," *IEEE Transactions on Power Electronics*, 2017, [Available online].

[11] S. Sinha, B. Regensburger, K. Doubleday, A. Kumar, S. Pervaiz, and K. Afridi, "High-power-transfer-density capacitive wireless power transfer system for electric vehicle charging," *Proceedings of the IEEE Energy Conversion Congress and Expo (ECCE),* Cincinnati, OH, Oct 2017.

[12] "Wireless Power Transfer for Light-Duty Plug-In/ Electric Vehicles and Alignment Methodology," SAE International J2954 Task Force, Surface Vehicle Information Report, 2016.

[13] International Commission on Non-Ionizing Radiation Protection, "Guidelines for limiting exposure to time-varying electric, magnetic, and electromagnetic fields (up to 300 GHz)." *Health Physics*, vol. 74, no. 4, pp. 494–522, 1998.

[14] S. Sinha, A. Kumar, S. Pervaiz, B. Regensburger, and K. K. Afridi, "Design of efficient matching networks for capacitive wireless power transfer systems," *Proceedings of the IEEE Workshop on Control and Modeling for Power Electronics (COMPEL),* Trondheim, Norway, pp. 1–7, June 2016.

[15] A. Kumar, S. Sinha, A. Sepahvand, and K. Afridi, "Improved design optimization for high-efficiency matching networks," *IEEE Transactions on Power Electronics*, 2017, [Available online].